Article

Antigen-Triggered Logic-Gating of DNA Nanodevices

Wouter Engelen, Christian Sigl, Karoline Kadletz, Elena M. Willner, and Hendrik Dietz*

Read Online

ACCESS | Metrics & More | Article Recommendations | Supporting Information

ABSTRACT: Synthetic nanoscale devices that reconfigure dynamically in response to physiological stimuli could offer new avenues for diagnostics and therapy. Here, we report a strategy for controlling the state of DNA nanodevices based on sensing antigens with IgG antibodies. To this end, we use IgG antibodies as structural elements to kinetically trap reconfigurable DNA origami structures in metastable states. Addition of soluble antigens displace the IgGs from the objects and triggers reconfiguration. We demonstrate this mechanism by antigen-triggered disassembly of DNA origami shells for two different IgGs and their cognate antigens, and we determined the corresponding dose response curves. We also describe the logic-gated actuation of DNA objects with combinations of antigens, as demonstrated with AND-type shells that disassemble only when two different antigens are detected simultaneously. We apply our system for the antigen-triggered release of molecular payload as exemplified by the release of virus particles that we loaded into the DNA origami shells. We expect our approach to be applicable in many types of DNA nanostructures and with many other IgG-antigen combinations.
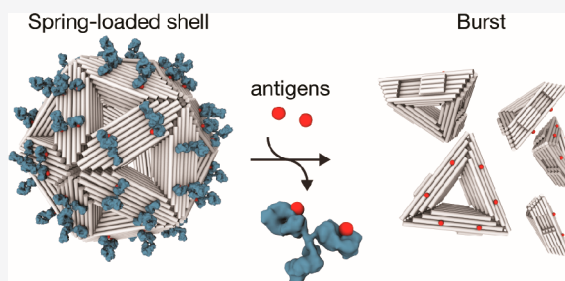
INTRODUCTION

Creating synthetic nanoscale devices that can respond to physiological stimuli is a long-standing goal of nucleic acid nanotechnology.[1−4] Such devices could be envisioned to accomplish advanced functions in diagnostics and therapy in an autonomous fashion, for example by executing preprogrammed actions such as the release of a molecular payload in response to the presence of user-defined antigens or metabolites. In the past, researchers have explored noncanonical shape-changing nucleic acid structures such as DNA triplexes or i-motifs to control the state of nanodevices as a function of pH.[5−7] Nucleic acid aptamers have also been employed as biochemical, ligand-specific shape-changing recognition elements[8,9] and used, for example, to control the reconfiguration of a DNA-based "nanorobot"[10,11] to enable cellular apoptosis or platelet aggregation in a logic-driven, autonomous fashion. These previous systems relied on a dynamic competition between ligand-dependent functional aptamer folds and the formation of duplex DNA motifs and depended on the availability of suitable aptamers.

The adaptive mammalian immune system provides a rich source of highly specific molecular recognition elements in the form of Immunoglobulin G (IgG) antibodies.[12] IgGs feature two identical binding sites for a target antigen, which can range from small molecules to macromolecules. Using monoclonal antibody generation techniques, high specificity and high affinity IgGs against nearly every target molecule can be systematically generated and harvested.[13,14] The bivalent display of identical antigen-binding sites has previously been used as a platform for dynamic DNA nanotechnology to control toehold mediated strand displacement reactions or DNA triplex−duplex equilibria.[15−17] IgGs undergo only modest conformational changes upon ligand binding, which means there is no obvious distance variable that could be directly coupled to a nanodevice to control its state.[18,19] Here, we present a system that can discriminate between monovalent and bivalent IgG-antigen binding state and exploits this variable to elicit molecular reconfiguration in synthetic DNA devices in response to the recognition of antigens by IgG antibodies.

RESULTS AND DISCUSSION

Our mechanism triggers device reconfigurations when IgG antibodies bind to cognate antigens. To accomplish this goal, we consider a switchable molecular device that displays pairs of antigens such that conformational changes of the device affect the spacing between the antigen pairs (Figure 1a, condition 1 vs condition 2). In one conformation the antigen pair spacing is compatible with bivalent IgG antibody binding, and in another it is not. In a first step, called IgG stapling, IgGs are brought into the system to dock onto the antigen pairs under conditions for which the antigen pair distance is compatible with bivalent IgG antibody binding (condition 2).[20,21] In a second step, called spring loading, the system is subjected to conditions where the molecular device would normally switch
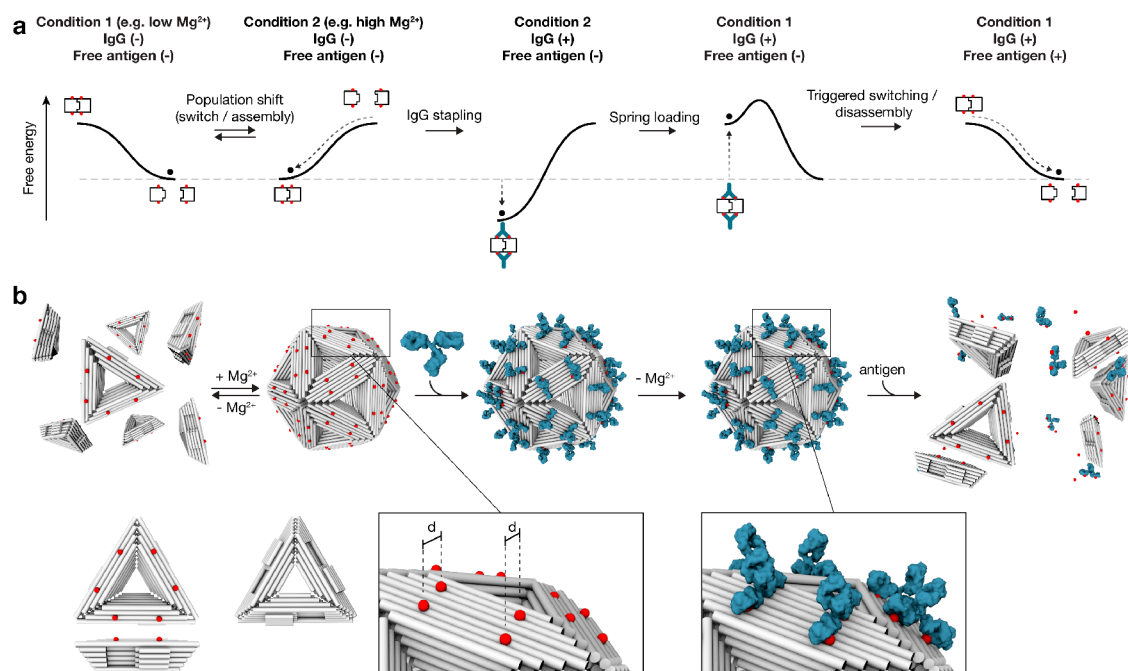
Figure 1. IgG mediated stabilization and antigen triggered disassembly of icosahedral DNA origami shells. (a) Schematic representation of the general principle of the antigen-detection mechanism, depicted in terms of the free energy of the system. (b) Schematic representation of a specific implementation to control the assembly state of DNA origami icosahedral shells using free antigens. Cylinders indicate double-helices. Red circles denote antigens. Blue y-shaped objects: IgG antibodies. Inset: length d refers to the pairwise antigen spacing.

to the conformation where the antigen spacing is no longer compatible with bivalent IgG binding (condition 1). However, in the presence of IgG staples, the system is kinetically trapped in a high-energy state through the bivalent IgG antibody locks. In this state, the mechanism is ready to sense and respond with a conformational change to the presence of antigens. This is because soluble antigens can displace the IgG antibodies, which removes the kinetic barrier for relaxation into the lower-energy state of the device.

In principle, our concept can be employed to control the conformation of many DNA objects featuring internal degrees of freedom in an antigen-dependent manner. However, it can also be employed to control the oligomerization state of higher-order DNA assemblies. For the present study, we decided to implement our antigen-sensing mechanism in a previously described icosahedral DNA origami shell system.[22] We will use this example to illustrate antigen-dependent logic-gated release of a molecular payload (a viral particle) from the shells.

The icosahedral shells form by self-assembly of 20 identical DNA origami triangle subunits that interact via shape-complementary blunt-end stacking. As for many other higher-order DNA assemblies of this type,[23,24] at low magnesium concentrations the equilibrium is shifted to monomers, whereas at high magnesium concentrations complete shells are favored (Figure 1b). Once shells are formed, we staple the triangle-triangle edges together with bivalent IgG antibody bridges formed between pairs of antigens. Neighboring triangle monomers each contribute one antigen to an antigen pair, i.e., each triangle contributes six antigens. Once the shells are stapled by IgG antibodies, the shells are returned to conditions for which they would disassemble ("burst") in the absence of the IgG staples. However, the shells cannot disassemble unless the antibodies dissociate. The shells are thus kinetically locked in a high-

energy "spring-loaded" state. The bursting of the shells can now be triggered by a user-defined biochemical stimulus in the form of soluble antigens that displace the IgG staples from the shells.

The spacing of antigen pairs has strong effects on the affinity of bivalent IgG binding, with optimal antigen spacing between 12 and 16 nm.[20,21] Based on a cryo-EM reconstruction of the assembled icosahedral shell in the presence of 25 mM $MgCl_2$ (EMDB: EMD-12024), we selected antigen-pair locations which yield antigen spacings of approximately 8.5 nm in the shell state (Figure S1). This spacing was chosen to accommodate for swelling of the DNA origami shell upon transfer to low counterion conditions, which has previously been observed for other DNA origami objects[25] and for an increase in the distance between triangular edge—edge contacts. Both effects increase the antigen spacing toward the optimum-affinity antigen spacing and the antibody—antigen staples are expected to tighten upon transferring the IgG-stapled shells to low ionic strength conditions.

We tested our concept exemplarily with digoxigenin and 2,4-dinitrophenol and their respective IgG antibodies. After shell assembly, we titrated the concentration of antidigoxigenin IgG against a fixed concentration of shells displaying the corresponding antigen pair. Electrophoretic mobility shift assays (Figure S2) indicated that a saturation of the antigen sites was achieved at six equivalents of IgG per triangle monomer, which corresponds to a ratio of 2:1 relative to available antibody docking sites. We also imaged the antibody-stapled icosahedral shells using cryo-electron microscopy (cryo-EM; Figures 2a and S3) and determined a 3D electron density map (Figure 2b). The cryo-EM map had an overall resolution of 23 Å and reveals a fully assembled icosahedral shell composed of 20 triangle monomers as expected by design. The docked IgG antibodies are clearly resolved in the map, and one may appreciate the comparably large size of the
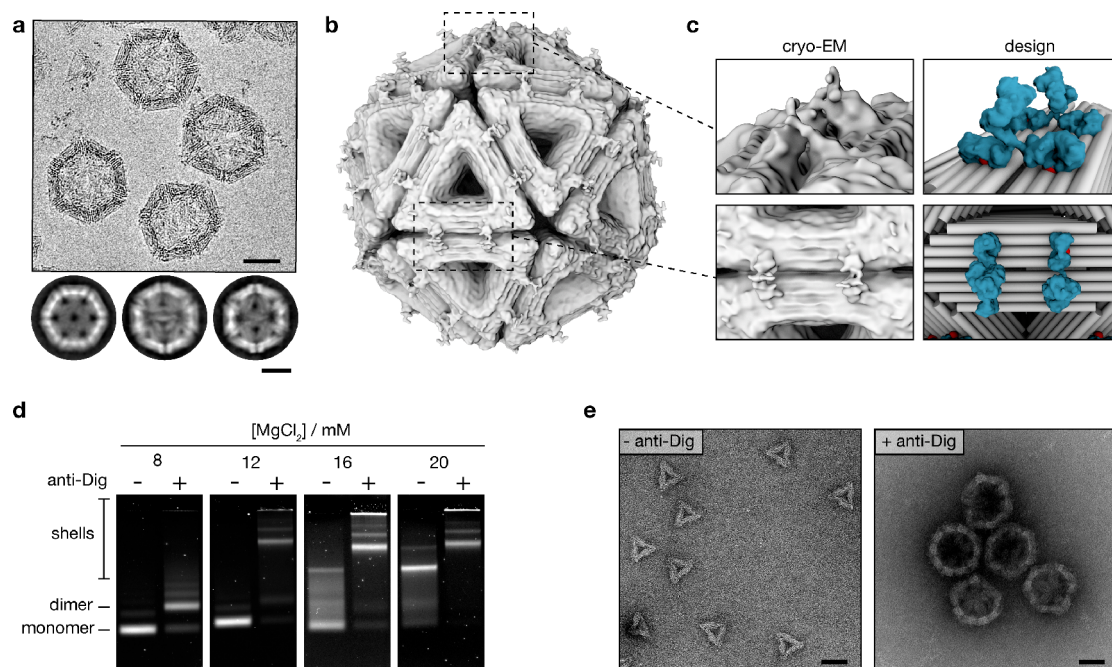
Figure 2. Structural characterization and evaluation of Mg^{2+} dependent IgG mediated shell stabilization. (a) Top: Exemplary Cryo-EM micrograph of icosahedral shells in free-standing ice with antidigoxigenin antibodies cross-linking the triangle-triangle interfaces at 25 mM $MgCl_2$. Bottom: Two-dimensional class averages showing the object from different orientations. (b) Cryo-EM reconstruction of the assembled icosahedral shell with two antidigoxigenin antibodies bridging each triangle-triangle interface (EMDB: EMD-13888). (c) Enlargement at a triangle-triangle interface cross-linked by two antidigoxigenin antibodies depicted in (left) a cryo-EM reconstruction and (right) a cylinder model with manually positioned IgG antibodies (PDB: 1IGT). Notably, in addition to both Fab fragments, parts of the antibody's Fc region are reconstructed. (d) Laser-scanned fluorescence images of 0.75% agarose gels in 0.5× TBE buffer supplemented with 8, 12, 16, and 20 mM $MgCl_2$. Assembled shells were incubated with and without antidigoxigenin antibodies at 25 mM $MgCl_2$ and subsequently diluted to the respective $MgCl_2$ concentrations and electrophorized on the corresponding gels. Monomer: single triangle monomers, dimer: dimers formed by 2 triangle subunits, shells: fully assembled shells. (e) Negatively stained TEM images of shells incubated without (left) or with (right) antidigoxigenin antibodies and diluted to 12 mM $MgCl_2$. Scale bar, 50 nm.

icosahedral shell relative to the IgG antibodies. One can also discern the inverted Y-shape of the IgGs, with the two antigen binding sites fixed to triangles and the Fc regions pointing away from the shell (Figure 2c).

EMSA band pattern analysis indicated that a suitable condition for spring-loading IgG stapled shells is attained in the presence of 12 mM $MgCl_2$ (Figure 2d). At this condition, icosahedral shells lacking IgG staples burst into monomers, whereas the IgG stapled shells remain intact. This finding is corroborated by TEM image data (Figure 2e). We note that the shells tended to cluster in the presence of IgGs (seen in EMSA as higher-order bands and in TEM), which we attribute to IgGs that bridge triangles within different shells rather than within the same shell. We expect that the optimal divalent ion concentration for spring-loading can be tuned by coating the shell monomers with varying ratios of oligolysine and PEG-oligolysine, as we have previously shown for higher order DNA origami assemblies.[26]

To trigger the bursting of the spring-loaded shells, it suffices to add the corresponding free antigen to solution, which we tested here for shells stapled by antidigoxigenin or antidinitrophenol IgGs (Figure 3a,d). EMSA (Figure 3b,e, top) revealed an increase of monomers for increasing concentration of soluble antigen together with a decrease of intact shells. TEM images (Figure 3b,e, bottom) showed intact shells in the absence of antigen and only triangle monomers in the presence of antigen at a sufficiently high concentration. To determine the dose response curves, we performed FRET efficiency

measurements. To this end, we mounted dyes (Cy3 and Cy5) at equal distances from the symmetry axes at all three sides of the triangle monomers. In this configuration, intact shells will give high FRET signals, while disassembled shells (i.e., triangle monomers) give low FRET efficiencies, which we indeed observed (Figure 3c,f). From the observed FRET ratios, we derived the fraction of assembled shells present in solution. Analysis of the data by fitting a Hill-Langmuir equation gives a half maximal effective concentration (EC_{50}) of 1.2 ± 0.1 μM for digoxigenin and 280 ± 24 μM for dinitrophenol. The measured EC_{50} for dinitrophenol is significantly higher compared to the digoxigenin antibody—antigen pair, even though their reported bulk affinities are similar (2.9 nM vs 3.5 nM, respectively).[27,28] We attribute this effect to the different chemical structure and local environment of the shell-mounted dinitrophenol compared to the free antigen, which has previously been shown to have significant effects on the antibody-dinitrophenol dissociation constant.[27] The Hill-coefficient was in both cases 1.7 ± 0.2. The Hill-coefficient indicates positive cooperativity, which suggests that displacement of one antibody from the shell promotes the displacement of subsequent antibodies.

Our antigen sensing mechanism by IgG-stapled spring-loaded objects can also be employed in a combinatorial fashion to implement molecular logic, for example to create an AND gate that responds to two antigens. To demonstrate this option, we assembled and IgG stapled shells that display two types of antigen pairs (Figure 3g). Adding either free
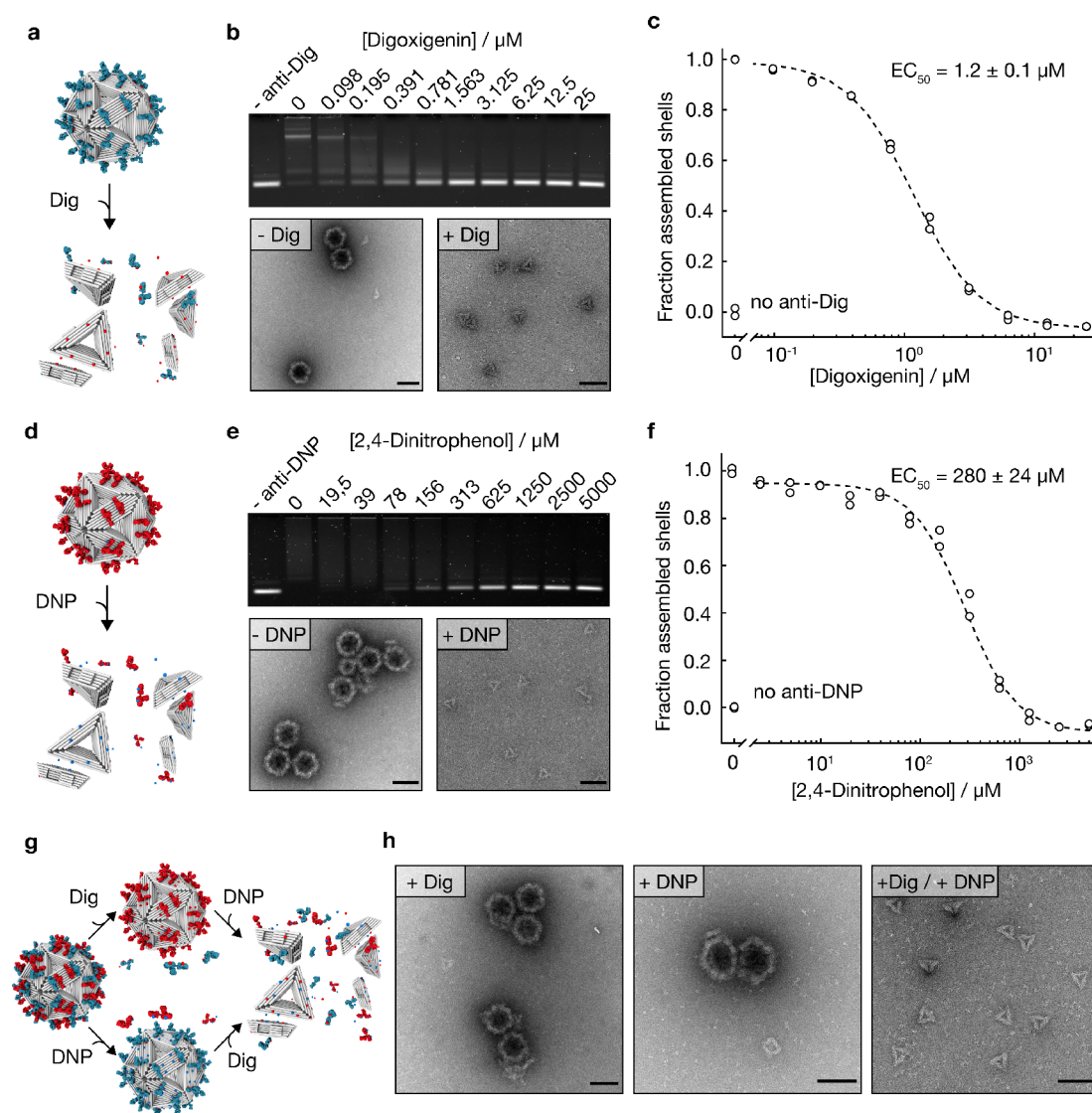
Figure 3. Antigen-triggered disassembly of icosahedral shells. (a) Scheme showing the addition of soluble digoxigenin ligands to compete off shell-stabilizing antidigoxigenin antibodies, which triggers disassembly of the shell. (b) Top: Laser-scanned fluorescence images of 0.75% agarose gels in 0.5× TBE buffer supplemented with 12 mM MgCl$_2$. Assembled shells equipped with antidigoxigenin antibodies were incubated with increasing concentrations of digoxigenin. Antidigoxigenin stabilized shells disassemble at increasing concentrations of soluble digoxigenin antigens. Bottom: Negative-staining TEM images of antidigoxigenin stabilized shells in absence (left) and presence (right) of 25 μM soluble digoxigenin. (c) Normalized FRET ratio of shells stabilized by antidigoxigenin at increasing concentrations of soluble digoxigenin ligands. The dashed lines represent nonlinear least-squares optimization of the Hill-Langmuir equation to the experimental data. (d−f) Similar as in panel a but with anti-dinitrophenol stabilized shells and addition of soluble 2,4-dinitrophenol ligand. (g) AND-gate logic gated shell disassembly is realized by installing both digoxigenin and 2,4-dinitrophenol ligands and the respective antibodies on the triangle-triangle interfaces. Disassembly of the AND-gate shell consequently requires the presence of both soluble digoxigenin and 2,4-dinitrophenol. (h) Negative-staining TEM images of shells equipped with antidigoxigenin and anti-dinitrophenol incubated with left: 25 μM digoxigenin; middle: 5 mM 2,4-dinitrophenol; and right: 25 μM digoxigenin and 5 mM 2,4-dinitrophenol. Scale bars, 100 nm.

digoxigenin or 2,4-dinitrophenol alone did not result in the bursting of the shells, as seen, e.g., by TEM imaging (Figure 3h). Only once both antigens are added to solution the spring-loaded shells burst into monomers, confirming the desired AND-gated mechanism (Figure 3h).

As a proof-of-concept for antigen-triggered release of molecular payload, we packed the shells with Hepatitis B virus (HBV) core particles. To this end, we functionalized a fraction of the triangle monomers at their shell-inward-facing surface with single stranded DNA extensions, to which we hybridized an HBV-specific antibody covalently tagged with a complementary DNA strand (Figure 4a). Adding HBV core

particles during shell assembly resulted in shells containing a viral cargo fixed to the shell walls (Figure 4b). The internal cavity permits accommodating multiple viral particles, as is clearly visible by negatively stained TEM imaging. We then removed the anti-HBV antibody from the shell interior via strand displacement, leading to freely floating but sterically trapped viral cargo. We stapled the shells with IgG antibodies and transferred them to low-ionic strength conditions for spring loading (Figure 4c, Figure S4). Addition of soluble digoxigenin then triggered the bursting of the DNA origami shell, leading to the release of the viral cargo (Figure 4d).
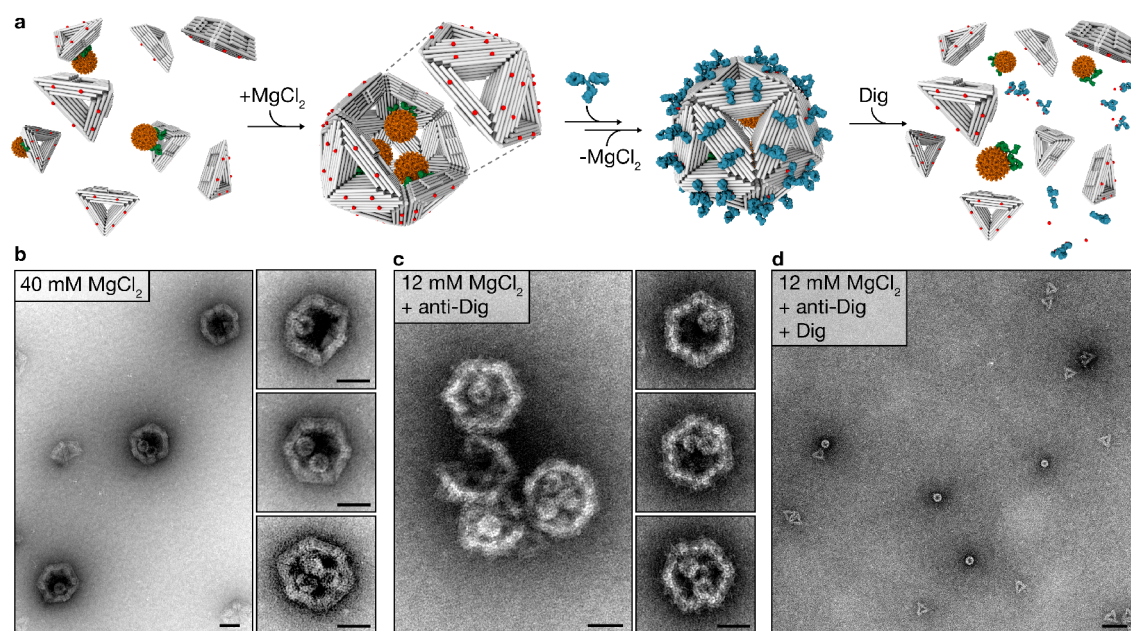
Figure 4. Antigen-triggered release of viral payload. (a) Scheme showing (from left to right) the functionalization of a subset of triangles with Hepatitis B virus core capsids, where the binding of the HBV particles is mediated by specific antibodies at the triangle's shell-inward-facing surface; assembly of complete shells with HBV core capsids in the lumen; stapling by anti-Dig IgG antibodies and spring-loading by reduction of ionic strength; antigen-triggered shell bursting and release of the viral payload by adding soluble digoxigenin antigens. Not shown is an intermediate step in which the HBV-binding antibodies located at the shell interior are detached from the shells, to have HBV particles freely floating in the shells. (b−d) Negatively staining TEM images of shells assembled at 40 mM MgCl$_2$ in the presence of viral payload, anti-Dig stapled shells packed with viral payload under spring-loading conditions (12 mM MgCl$_2$, see Figure S4 for additional images), shells disassembled by adding soluble digoxigenin antigens, leading to the release of the viral payload, respectively. Scale bar 50 nm (b and c) and 100 nm (d).

■ CONCLUSION

In conclusion, we successfully tested two specific antibody−antigen pairs as a structural element in spring-loaded DNA origami objects. The modularity of the system should allow swapping in other antibody−antigen pairs. The mechanisms worked with different locations for mounting the antigens on the object without the need for finetuning. This suggests that the mechanism is robust and will function as long as the simple antigen-spacing criteria described in Figure 1A are satisfied. We thus anticipate that many other switchable DNA devices, mechanisms, and higher-order assemblies can be turned into antigen-detecting molecular sensors using our mechanism. The spring-loaded antigen sensitive state is a fully integrated unimolecular object, which is important for applications under dilute conditions such as in molecular diagnostics or therapeutics.

Furthermore, our shells that can be programmed to burst and release a viral cargo in response to antigens illustrate future avenues for antigen-controlled drug delivery. For example, instead of responding to soluble antigens, the shell could presumably be programmed to burst upon recognizing certain cell surface markers. This could be realized by placing pairs of cell receptor domains or pairs of peptide fragments on the shells and stapling the shells using the corresponding IgGs. In this way, the shells would become agents featuring an integrated cell targeting and release control mechanism. We chose to release a viral cargo in our experiments as an illustration for a therapeutic payload. This choice was motivated by ongoing efforts in developing oncolytic viruses for cancer treatment,[29] but directing those therapeutic viruses to tumor cells is a major challenge. Our shells and the release mechanism may provide a solution to this problem.

■ EXPERIMENTAL SECTION

Folding of DNA Origami Objects. The $T = 1$ DNA origami triangles were folded in a one-pot folding reaction as described previously.[30] In short, 50 nM of a M13-derived 8064 bases long circular scaffold strand and 200 nM of each staple strand (see Supporting Information, notes 1and 2 for sequences and Figure S5 for design diagram) were subjected to a thermal annealing ramp in a Tetrad (Bio-Rad) thermal cycling device (65 °C for 15 min, 58−54 °C with a decrease of 1 °C/1 h, stored at 20 °C). The folding reaction was performed in standardized "folding buffer" (5 mM Tris Base, 1 mM EDTA, 5 mM NaCl, pH 8) containing 20 mM MgCl$_2$ (FoB20). The scaffold was produced as previously described,[31,32] and staples were purchased from IDT (Integrated DNA Technologies). Digoxigenin and dinitrophenol functionalized oligonucleotides were purchased from Biomers.net.

Purification of Shell Subunits and Self-Assembly of Shells. All DNA-origami triangles were purified using agarose gel purification and if necessary concentrated by ultrafiltration as reported previously[30,33] with the following changes. For gel purification, gels containing 1.5% agarose, 0.5× TBE buffer (22.25 mM Tris Base, 22.25 mM Boric Acid, 0.5 mM EDTA) and 5.5 mM MgCl$_2$ were used. For ultrafiltration, gel purified sample was added to the same filter multiple times (2−5 times). This was followed by 2 washing steps with FoB5 to accurately control buffer conditions. To assemble the triangles into shells, the MgCl$_2$ concentration was adjusted to 25 mM unless stated otherwise and the sample was incubated at 40 °C for at least 1 day. Typical triangle concentrations were in a range of 5 to 100 nM.

***T* = 1 Shell Antibody Stabilization and Antigen-Triggered Disassembly.** The $T = 1$ triangles were equipped with two digoxigenin-modified DNA-strands and/or two DNP-modified DNA-strands per triangle side (Figure S1), which were included in the one-pot folding reaction. Additionally, per triangle side one Cy3 and one Cy5 fluorophore were introduced to facilitate FRET readout for shell disassembly (Figure S1). The triangles were purified and assembled as described above. Five μL fully assembled shells in FoB25

were mixed with 2.5 μL of 120 nM antidigoxigenin (Mouse monoclonal IgG1κ, clone: 1.71.256) in FoB22.5 + 0.05% Tween-20 and/or 2.5 μL of 120 nM antidinitrophenol (rat monoclonal IgG1κ, clone: LO−DNP-2) in FoB22.5 + 0.05% Tween-20 and incubated for 2 h at 25 °C. When only a single antibody type was added the omitted antibody was substituted by 2.5 μL of FoB22.5 + 0.05% Tween-20. Subsequently, the MgCl$_2$ concentration was decreased to 12 mM by adding 40 μL of FoB9 + 0.05% Tween-20 and 2.5 μL of various concentrations of digoxigenin and/or 2,4-dinitrophenol in FoB22.5 + 0.05% Tween-20. FRET was measured in a 384 well plate on a platereader pre-equilibrated to 30 °C (CLARIOstar, BMG labtech, λ_{ex} = 530 ± 10 nm, $\lambda_{em,A}$ = 675 ± 25 nm and $\lambda_{em,D}$ = 580 ± 15 nm). All experiments were performed in duplicates.

Agarose Gel Electrophoresis. Agarose gel electrophoresis was used to evaluate the size distribution of the shell assembly. The samples were loaded on gels containing 0.75% agarose, 0.5× TBE buffer (22.25 mM Tris Base, 22.25 mM Boric Acid, 0.5 mM EDTA) and a MgCl$_2$ concentration as indicated in the figure captions. EtBr was added to gels containing DNA-origami triangles without fluorescent dyes to visualize the structures. For MgCl$_2$ concentrations higher than 15 mM, a surrounding ice-cooled water bath was used, and the buffer was exchanged every 45 min. Gel electrophoresis was performed for 1.5 to 2 h at a bias voltage of 90 V. The gels were scanned with a Typhoon FLA 9500 laser scanner (GE Healthcare) with a pixel size of 50 μm/pixel.

Negatively Stained TEM. A total of 5 μL of the sample was incubated (30−120 s) on plasma-treated Formvar-supported carbon-coated Cu400 TEM grids (Electron Microscopy Science). The grids were washed with 5 μL of 2% aqueous uranyl formate solution containing 25 mM sodium hydroxide and subsequently stained with 20 μL of the same stain solution for 30 s. TEM images were acquired with a FEI Tecnai T12 microscope operated at 120 kV with a Tietz TEMCAM-F416 camera at a typical magnification of 10 000× to 52 000× with SerialEM. Images were high-pass filtered and autoleveled with Adobe Photoshop.

Cryo Electron Microscopy. Triangle monomers were concentrated to 100 nM, assembled into icosahedral shells, and antibody-stapled as described above. Then 3 μL of the sample was added to plasma-treated C-flat 1.2/1.3 grids (Protochip) and plunge-frozen in liquid ethane with a Vitrobot Mark V (2 s blot time, −1 blot force, 0 s drain and wait time). The temperature and humidity were set to 22 °C and 100%, respectively. Micrographs were acquired with a Cs-corrected Titan Krios G2 electron microscope (Thermo Fisher) operated at 300 kV and equipped with a Falcon III 4k direct electron detector (Thermo Fisher). Images were acquired at a defocus of −2 μm, with a pixel size of 2.9 Å/pixel, 18 fractions, and a dose of 42 e/Å^2. Image processing was done in RELION3.[34,35] The movies aligned with MotionCor2[36] and CTF estimation performed using CTFFIND4.1.[37] Particles were selected through visual inspection in multiple rounds of 2D and 3D classifications. The initial model was calculated in RELION3. In total 629 particles were used for the refinement using icosahedral symmetry (I1).

Viral Particle Loading and Disassembly. Triangles with three additional staple-extensions for the attachment of anti-HBVc-DNA conjugates were folded and purified as described above. Anti-HBVc-DNA conjugates were prepared and purified as reported in ref 30, added to purified triangles in a 1:1 ratio relative to attachment sites on the triangles, and incubated for 2 h at room temperature. Triangles functionalized with and without anti-HBVc were mixed with HBVc particles at a total triangle concentration of 8 nM (4 nM triangles with and 4 nM triangles without anti-HBVc) and incubated in FoB5 for 2 h before increasing the MgCl$_2$ concentration to 40 mM and incubating the sample at room temperature for 1 day to allow shell assembly. To detach anti-HBVc-DNA conjugates from the shell's interior surface and trigger the disassembly of spring-loaded shells, 8 μL of shells were mixed with 2 μL of displacer oligonucleotide (50 μM, Supporting Information, note 2) and 2 μL of digoxigenin (68.4 μM) at a MgCl$_2$ concentration of 40 mM and incubated for 1.5 h at room temperature. For negative control samples, 2 μL of FoB40 was added instead of digoxigenin. Finally, the samples were diluted to a MgCl$_2$

concentration of 12 mM by mixing 2 μL of sample with 8 μL of FoB5. Negative stain grids were prepared after 1 h incubation at a MgCl$_2$ concentration of 12 mM as described above.

ASSOCIATED CONTENT

Ⓢ Supporting Information

The Supporting Information is available free of charge at https://pubs.acs.org/doi/10.1021/jacs.1c09967.

Schematic representation of antigen placement on DNA origami monomers, EMSA of anti-digoxigenin titration, Cryo-EM reconstruction of antidigoxigenin stabilized shell, negative stained TEM images of HBVc encapsulating shells, and design diagram of DNA origami triangle monomer (PDF)

AUTHOR INFORMATION

Corresponding Author

Hendrik Dietz − *Laboratory for Biomolecular Nanotechnology, Physics Department and Munich Institute of Biomedical Engineering, Technical University of Munich, Garching near Munich 85748, Germany*; Email: dietz@tum.de

Authors

Wouter Engelen − *Laboratory for Biomolecular Nanotechnology, Physics Department and Munich Institute of Biomedical Engineering, Technical University of Munich, Garching near Munich 85748, Germany*; ⓞ orcid.org/0000-0001-8779-9887

Christian Sigl − *Laboratory for Biomolecular Nanotechnology, Physics Department and Munich Institute of Biomedical Engineering, Technical University of Munich, Garching near Munich 85748, Germany*

Karoline Kadletz − *Laboratory for Biomolecular Nanotechnology, Physics Department and Munich Institute of Biomedical Engineering, Technical University of Munich, Garching near Munich 85748, Germany*

Elena M. Willner − *Laboratory for Biomolecular Nanotechnology, Physics Department and Munich Institute of Biomedical Engineering, Technical University of Munich, Garching near Munich 85748, Germany*

Complete contact information is available at:
https://pubs.acs.org/10.1021/jacs.1c09967

Notes

The authors declare the following competing financial interest(s): A provisional patent has been filed by the TUM.

Journal of the American Chemical Society
pubs.acs.org/JACS
Article

only. The EU Commission takes no responsibility for any use made of the information set out.

■ REFERENCES

(1) Shen, L.; Wang, P.; Ke, Y. DNA Nanotechnology-Based Biosensors and Therapeutics. *Adv. Healthcare Mater.* **2021**, *10*, 2002205.

(2) Chen, Y. J.; Groves, B.; Muscat, R. A.; Seelig, G. DNA nanotechnology from the test tube to the cell. *Nat. Nanotechnol.* **2015**, *10* (9), 748−60.

(3) Ramezani, H.; Dietz, H. Building machines with DNA molecules. *Nat. Rev. Genet.* **2020**, *21* (1), 5−26.

(4) Hong, F.; Zhang, F.; Liu, Y.; Yan, H. DNA Origami: Scaffolds for Creating Higher Order Structures. *Chem. Rev.* **2017**, *117* (20), 12584−12640.

(5) Ijäs, H.; Hakaste, I.; Shen, B.; Kostiainen, M. A.; Linko, V. Reconfigurable DNA Origami Nanocapsule for pH-Controlled Encapsulation and Display of Cargo. *ACS Nano* **2019**, *13* (5), 5959−5967.

(6) Wu, N.; Willner, I. pH-Stimulated Reconfiguration and Structural Isomerization of Origami Dimer and Trimer Systems. *Nano Lett.* **2016**, *16* (10), 6650−6655.

(7) Kim, S. H.; Kim, K.-R.; Ahn, D.-R.; Lee, J. E.; Yang, E. G.; Kim, S. Y. Reversible Regulation of Enzyme Activity by pH-Responsive Encapsulation in DNA Nanocages. *ACS Nano* **2017**, *11* (9), 9352−9359.

(8) Nutiu, R.; Li, Y. Structure-switching signaling aptamers. *J. Am. Chem. Soc.* **2003**, *125* (16), 4771−8.

(9) Hamaguchi, N.; Ellington, A.; Stanton, M. Aptamer beacons for the direct detection of proteins. *Anal. Biochem.* **2001**, *294* (2), 126−31.

(10) Douglas, S. M.; Bachelet, I.; Church, G. M. A logic-gated nanorobot for targeted transport of molecular payloads. *Science* **2012**, *335* (6070), 831−4.

(11) Li, S.; Jiang, Q.; Liu, S.; Zhang, Y.; Tian, Y.; Song, C.; Wang, J.; Zou, Y.; Anderson, G. J.; Han, J. Y.; Chang, Y.; Liu, Y.; Zhang, C.; Chen, L.; Zhou, G.; Nie, G.; Yan, H.; Ding, B.; Zhao, Y. A DNA nanorobot functions as a cancer therapeutic in response to a molecular trigger in vivo. *Nat. Biotechnol.* **2018**, *36* (3), 258−264.

(12) Parkin, J.; Cohen, B. An overview of the immune system. *Lancet* **2001**, *357* (9270), 1777−1789.

(13) Li, F.; Vijayasankaran, N.; Shen, A.; Kiss, R.; Amanullah, A. Cell culture processes for monoclonal antibody production. *mAbs* **2010**, *2* (5), 466−479.

(14) Birch, J. R.; Racher, A. J. Antibody production. *Adv. Drug Delivery Rev.* **2006**, *58* (5), 671−685.

(15) Engelen, W.; Meijer, L. H. H.; Somers, B.; de Greef, T. F. A.; Merkx, M. Antibody-controlled actuation of DNA-based molecular circuits. *Nat. Commun.* **2017**, *8* (1), 14473.

(16) Ranallo, S.; Prévost-Tremblay, C.; Idili, A.; Vallée-Bélisle, A.; Ricci, F. Antibody-powered nucleic acid release using a DNA-based nanomachine. *Nat. Commun.* **2017**, *8* (1), 15150.

(17) Ranallo, S.; Sorrentino, D.; Ricci, F. Orthogonal regulation of DNA nanostructure self-assembly and disassembly using antibodies. *Nat. Commun.* **2019**, *10* (1), 5509.

(18) Sela-Culang, I.; Alon, S.; Ofran, Y. A Systematic Comparison of Free and Bound Antibodies Reveals Binding-Related Conformational Changes. *J. Immunol.* **2012**, *189*, 4890.

(19) Stanfield, R. L.; Wilson, I. A. Antigen-induced conformational changes in antibodies: A problem for structural prediction and design. *Trends Biotechnol.* **1994**, *12* (7), 275−279.

(20) Shaw, A.; Hoffecker, I. T.; Smyrlaki, I.; Rosa, J.; Grevys, A.; Bratlie, D.; Sandlie, I.; Michaelsen, T. E.; Andersen, J. T.; Högberg, B. Binding to nanopatterned antigens is dominated by the spatial tolerance of antibodies. *Nat. Nanotechnol.* **2019**, *14* (2), 184−190.

(21) Zhang, P.; Liu, X.; Liu, P.; Wang, F.; Ariyama, H.; Ando, T.; Lin, J.; Wang, L.; Hu, J.; Li, B.; Fan, C. Capturing transient antibody conformations with DNA origami epitopes. *Nat. Commun.* **2020**, *11* (1), 3114.

(22) Sigl, C.; Willner, E. M.; Engelen, W.; Kretzmann, J. A.; Sachenbacher, K.; Liedl, A.; Kolbe, F.; Wilsch, F.; Aghvami, S. A.; Protzer, U.; Hagan, M. F.; Fraden, S.; Dietz, H. Programmable icosahedral shell system for virus trapping. *Nat. Mater.* **2021**, *20* (9), 1281−1289.

(23) Gerling, T.; Wagenbauer, K. F.; Neuner, A. M.; Dietz, H. Dynamic DNA devices and assemblies formed by shape-complementary, non−base pairing 3D components. *Science* **2015**, *347* (6229), 1446.

(24) Wagenbauer, K. F.; Sigl, C.; Dietz, H. Gigadalton-scale shape-programmable DNA assemblies. *Nature* **2017**, *552* (7683), 78−83.

(25) Gerling, T.; Kube, M.; Kick, B.; Dietz, H. Sequence-programmable covalent bonding of designed DNA assemblies. *Science Advances* **2018**, *4* (8), eaau1157.

(26) Bertosin, E.; Stömmer, P.; Feigl, E.; Wenig, M.; Honemann, M. N.; Dietz, H. Cryo-Electron Microscopy and Mass Analysis of Oligolysine-Coated DNA Nanostructures. *ACS Nano* **2021**, *15* (6), 9391−9403.

(27) Jung, H.; Yang, T.; Lasagna, M. D.; Shi, J.; Reinhart, G. D.; Cremer, P. S. Impact of Hapten Presentation on Antibody Binding at Lipid Membrane Interfaces. *Biophys. J.* **2008**, *94* (8), 3094−3103.

(28) Kong, J.; Bell, N. A. W.; Keyser, U. F. Quantifying Nanomolar Protein Concentrations Using Designed DNA Carriers and Solid-State Nanopores. *Nano Lett.* **2016**, *16* (6), 3557−3562.

(29) Fukuhara, H.; Ino, Y.; Todo, T. Oncolytic virus therapy: A new era of cancer treatment at dawn. *Cancer Sci.* **2016**, *107* (10), 1373−1379.

(30) Sigl, C.; Willner, E. M.; Engelen, W.; Kretzmann, J. A.; Sachenbacher, K.; Liedl, A.; Kolbe, F.; Wilsch, F.; Aghvami, S. A.; Protzer, U.; Hagan, M. F.; Fraden, S.; Dietz, H. Programmable icosahedral shell system for virus trapping. *Nat. Mater.* **2021**, *20*, 1281−1289.

(31) Engelhardt, F. A. S.; Praetorius, F.; Wachauf, C. H.; Brüggenthies, G.; Kohler, F.; Kick, B.; Kadletz, K. L.; Pham, P. N.; Behler, K. L.; Gerling, T.; Dietz, H. Custom-Size, Functional, and Durable DNA Origami with Design-Specific Scaffolds. *ACS Nano* **2019**, *13* (5), 5015−5027.

(32) Kick, B.; Praetorius, F.; Dietz, H.; Weuster-Botz, D. Efficient Production of Single-Stranded Phage DNA as Scaffolds for DNA Origami. *Nano Lett.* **2015**, *15* (7), 4672−4676.

(33) Wagenbauer, K. F.; Engelhardt, F. A. S.; Stahl, E.; Hechtl, V. K.; Stömmer, P.; Seebacher, F.; Meregalli, L.; Ketterer, P.; Gerling, T.; Dietz, H. How We Make DNA Origami. *ChemBioChem* **2017**, *18* (19), 1873−1885.

(34) Kimanius, D.; Forsberg, B. O.; Scheres, S. H. W.; Lindahl, E. Accelerated cryo-EM structure determination with parallelisation using GPUs in RELION-2. *eLife* **2016**, *5*, No. e18722.

(35) Zivanov, J.; Nakane, T.; Forsberg, B. O.; Kimanius, D.; Hagen, W. J. H.; Lindahl, E.; Scheres, S. H. W. New tools for automated high-resolution cryo-EM structure determination in RELION-3. *eLife* **2018**, *7*, No. e42166.

(36) Zheng, S. Q.; Palovcak, E.; Armache, J.-P.; Verba, K. A.; Cheng, Y.; Agard, D. A. MotionCor2: anisotropic correction of beam-induced motion for improved cryo-electron microscopy. *Nat. Methods* **2017**, *14* (4), 331−332.

(37) Rohou, A.; Grigorieff, N. CTFFIND4: Fast and accurate defocus estimation from electron micrographs. *J. Struct. Biol.* **2015**, *192* (2), 216−221.